



A novel reduced graphene oxide/Ag/CeO₂ ternary nanocomposite: Green synthesis and catalytic properties



Zhenyuan Ji^{a,b}, Xiaoping Shen^{a,*}, Jinglei Yang^a, Guoxing Zhu^a, Kangmin Chen^b

^a School of Chemistry and Chemical Engineering, Jiangsu University, Zhenjiang 212013, People's Republic of China

^b School of Materials Science and Engineering, Jiangsu University, Zhenjiang 212013, People's Republic of China

ARTICLE INFO

Article history:

Received 23 April 2013

Received in revised form 1 July 2013

Accepted 21 July 2013

Available online 31 July 2013

Keywords:

Graphene
Cerium oxide
Silver
Synthesis
Catalysis

ABSTRACT

The incorporation of two or more active components onto graphene with uniform distribution is expected to facilitate wider applications of graphene-based materials. In this study, a three-component composite composed of reduced graphene oxide (RGO), CeO₂ and Ag nanoparticles was designed and synthesized by a facile and environmentally friendly strategy for the first time. It is shown that Ag and CeO₂ nanoparticles are uniformly deposited on the surface of RGO sheets. The catalytic properties of the RGO/Ag/CeO₂ ternary hybrid nanomaterials were evaluated with the reduction of *p*-nitrophenol by NaBH₄ as a model reaction. The results reveal that the presence of CeO₂ not only has a great influence on the size of the Ag nanoparticles formed on RGO, but also can significantly improve the catalytic activity and stability of them. Possible mechanisms for the reduced size of Ag nanoparticles and the enhanced catalytic performance of RGO/Ag nanocomposites after combining with CeO₂ were proposed. The facile synthesis of RGO/Ag/CeO₂ nanomaterials together with their superior catalytic performance provides a potentially new approach for the design and construction of graphene-based ternary nanostructured composites with various functions.

© 2013 Elsevier B.V. All rights reserved.

1. Introduction

Noble metal nanoparticles have been a focus of intensive research in recent years due to their unique optical, electronic and catalytic properties, which make them be suitable materials for potential applications in various fields [1–6]. Among them, silver (Ag) nanoparticles are particularly attractive because of the relatively low cost and distinctive properties such as superior conductivity, chemical stability, antimicrobial and plasmon-resonant optical scattering properties [7–9]. In particular, Ag nanoparticles have also been proven to be promising candidates in catalysis, and many excellent catalysts based on Ag nanoparticles have been reported [10]. The specific catalytic properties of Ag nanoparticles are directly related to their sizes and dispersion [11]. Highly dispersed Ag nanoparticles with small size are ideal for high catalytic performance owing to their large surface area [12]. However, their high surface energy due to the large surface area causes serious stability problems, such as a tendency to aggregate, changes in shape and damage to their surface states during catalytic reactions, and eventual loss of their original catalytic activities [13,14]. Therefore, important factors in utilizing Ag nanoparticles are how

to stabilize them to avoid their aggregation into large clusters and how to control their spatial positions in the materials. Additionally, considering their limited supply, the reduction of the used amounts and the increase of the recycling are highly expected for Ag nanoparticles.

In order to solve the above problems, an effective strategy is to immobilize Ag nanoparticles on the surface of solid supports with low cost, high surface area, and good chemical and physical properties. Up to now, Ag nanoparticles have been immobilized onto various supports such as chitosan [15], silica [16], alumina [17], zeolite [18], ceria [19], titania [20], activated carbon [21] and carbon nanotube [22], etc. Recently, the emergence of graphene has opened up an exciting new field in the science and technology with continuously growing academic and technological impetus [23,24]. Owing to its unique two dimensional structure and extraordinary physicochemical properties such as large surface area [25–27], excellent electrical conductivity and high chemical stability [28,29], graphene is considered as an ideal two dimensional carbon support for developing highly efficient catalysts [30,31]. It was reported that loading Ag nanoparticles onto graphene can not only prevent graphene sheets from restacking and expand the application areas of graphene, but also improve the catalytic performance of Ag nanoparticles owing to the strong synergistic effect between the two components [32–34]. Up to now, considerable attention has been paid on the synthesis of graphene oxide (GO)/Ag and reduced

* Corresponding author. Tel.: +86 511 84401889; fax: +86 511 88791800.
E-mail address: xiaopingshen@163.com (X. Shen).

graphene oxide (RGO)/Ag hybrid materials. However, despite the significant efforts, there still exist some challenges and problems in the study of graphene/Ag nanocomposites: (i) many of the synthesis approaches to graphene/Ag nanocomposites suffer from the use of hazardous or toxic reducing agents such as NaBH_4 and formaldehyde to reduce both GO and Ag^+ , posing environmental and health risks [35]. (ii) Some drawbacks such as uneven sizes and poor dispersion of Ag nanoparticles exist in the reported graphene/Ag cases, which result in a low stability and reproducibility in catalytic activity of graphene/Ag nanocomposites [36]. Thus, it is desirable to develop a facile and environmentally friendly route that produces well-dispersed Ag nanoparticles with good controllability and high dispersivity.

The incorporation of two or more active components onto graphene with excellent particle dispersivity is expected to facilitate wider applications of graphene-based nanocomposites [37–39]. Very recently, we have developed a self-assembly approach to synthesize CeO_2 nanoparticles with excellent dispersivity and good affinity to RGO by using poly(vinylpyrrolidone) (PVP) as a linker [40]. Inspired by it, in this work, we have fabricated a three-component nanocomposite system composed of RGO, CeO_2 and Ag nanocrystals through an environmentally friendly two-step synthesis strategy for the first time. Using this method, we can routinely produce RGO/Ag/ CeO_2 ternary nanomaterials with good dispersion and homogeneous distribution of Ag and CeO_2 nanoparticles on RGO without obvious interference or site competition between the Ag and CeO_2 nanoparticles. Furthermore, we demonstrate the catalytic application of the ternary nanocomposites in the catalytic reduction of *p*-nitrophenol into *p*-aminophenol by NaBH_4 .

2. Experimental

2.1. Materials

Natural flake graphite was purchased from Qingdao Guyu Graphite Co., Ltd., with a particle size of $150\ \mu\text{m}$ (99.9% purity). All of the other chemical reagents used in our experiments are of analytical grade, and used without further purification.

2.2. Synthesis of graphite oxide

Graphite oxide was prepared from the natural flake graphite according to the modified Hummers method [41,42]. In a typical synthesis, 2.0 g of graphite powder was added to 80 mL of cold (0°C) concentrated H_2SO_4 in an ice bath. Then, NaNO_3 (4.0 g) and KMnO_4 (8.0 g) were added gradually under stirring and the temperature of the mixture was maintained below 10°C . The reaction mixture was continually stirred for 4 h at temperature below 10°C . Successively, the mixture was stirred at 35°C for 4 h, and then diluted with 200 mL of deionized (DI) water. After adding DI water, the mixture was stirred for 1 h. The reaction was then terminated by adding 15 mL of 30% H_2O_2 solution. The solid product was separated by centrifugation and washed repeatedly with 5% HCl solution until sulfate could not be detected with BaCl_2 . For further purification, the resulting solid was re-dispersed in DI water and dialyzed for 3 days to remove any residual salts and acids. The suspension was dried in a vacuum oven at 45°C for 48 h to obtain graphite oxide.

2.3. Synthesis of RGO/Ag/ CeO_2 nanocomposites

6-Aminohexanoic acid (AHA)-stabilized CeO_2 nanoparticles was prepared according to our previous report [40]. Briefly, a solution containing 0.87 g of $\text{Ce}(\text{NO}_3)_3 \cdot 6\text{H}_2\text{O}$ and 80 mL of DI water was heated to 95°C under magnetic stirring, into which 8 mL of AHA

aqueous solution (containing 1.05 g of AHA) and $40\ \mu\text{L}$ of 37 wt% HCl solution were added in sequence. The resultant solution was then kept at 95°C for 6 h, and a homogeneous dispersion containing positively charged CeO_2 nanocrystals was obtained.

As a typical procedure to synthesize the RGO/Ag/ CeO_2 nanocomposites, 50 mg of PVP and 40 mg of graphite oxide were dispersed in 80 mL of DI water with ultrasonication for 30 min. Subsequently, a certain amount of CeO_2 dispersion was slowly added in, followed by vigorous stirring for 4 h. Five milliliters of AgNO_3 aqueous solution (containing 20 mg of AgNO_3) was then added to the above solution. After stirring for another 2 h, 5 mL of 0.5 M NaOH aqueous solution was added dropwise. The resulting mixture was then transferred into a 250 mL round-bottomed flask and refluxed at 95°C for 1 h. The solid products were separated by centrifugation, washed thoroughly with water and ethanol to remove any impurities, and then dried in a vacuum oven at 50°C for 24 h. The obtained products were designated as RGO/Ag/ CeO_2 -1, RGO/Ag/ CeO_2 -2, RGO/Ag/ CeO_2 -3 and RGO/Ag/ CeO_2 -4 for the feeding amount of 1, 2, 3 and 4 mL of CeO_2 dispersion, respectively. As a comparison, RGO/ CeO_2 and RGO/Ag were synthesized in the same way as the RGO/Ag/ CeO_2 -3 nanocomposites in the absence of AgNO_3 and CeO_2 , respectively. Bare RGO was also synthesized under the same conditions in the absence of both AgNO_3 and CeO_2 .

2.4. Instrumentation and measurements

The morphology and structure of the products were determined by transmission electron microscopy (TEM, JEOL JEM-2100) and powder X-ray diffraction (XRD, Bruker D8 ADVANCE) with Cu $K\alpha$ radiation. Samples for TEM observation were prepared by dropping the products on a carbon-coated copper grid after ultrasonic dispersion in absolute ethanol and allowed them to dry in air before analysis. The loading amounts of Ag in the RGO/Ag/ CeO_2 nanocomposites were evaluated by an inductively coupled plasma-optical emission spectrometer (ICP-OES, Vista-MXP, Varian). Fourier transform infrared (FT-IR) spectra were recorded on a Nicolet Nexus 470 spectrometer with KBr pellets in the 4000 – $400\ \text{cm}^{-1}$ region. Raman spectra were carried out at room temperature using a DXR Raman microscope with 532 nm excitation source from an Ar^+ laser. Ultraviolet-visible (UV-vis) spectroscopy measurements were performed on a UV-2450 ultraviolet-visible spectrophotometer.

2.5. Catalytic reduction of *p*-nitrophenol

The reduction reaction of *p*-nitrophenol by NaBH_4 was used as a model system to quantitatively evaluate the catalytic activity of the as-synthesized nanocomposites. In a typical procedure, the aqueous solutions of *p*-nitrophenol (10 mM) and NaBH_4 (1.5 M) were freshly prepared, respectively. Two milliliters of NaBH_4 solution was mixed with 200 mL of DI water under magnetic stirring in a 250 mL beaker at room temperature. A certain amount of catalysts with the same amount of Ag was then added to the above solution. After stirring for about 15 min, 1.5 mL of *p*-nitrophenol solution was injected into the mixture to start the reaction. The color of the solution changed from colorless to yellow immediately. During the reaction process, 2 mL of the reaction solution was quickly withdrawn from the reaction system at a regular time interval of 2 min, followed by measuring UV-vis spectra of the solution to monitor the concentration of *p*-nitrophenol through its absorption peak at 400 nm. For successive recycling of the catalysts in the catalytic reduction of *p*-nitrophenol, the measured reaction solutions were collected and mixed with remnant solution in the beaker. After that, 2 mL of freshly prepared NaBH_4 solution and 1.5 mL of *p*-nitrophenol solution were added to start the next round of reaction.

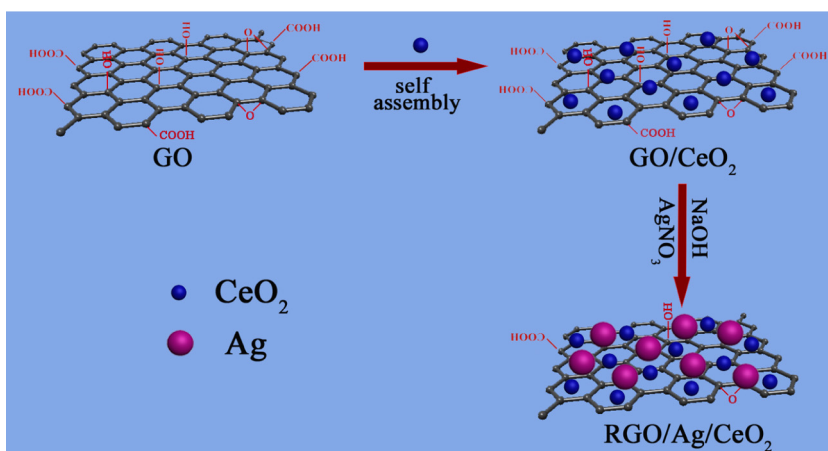


Fig. 1. Schematic illustration for the syntheses of RGO/Ag/CeO₂ nanocomposites.

3. Results and discussion

3.1. Synthesis of RGO/Ag/CeO₂ nanocomposites

A two-step routine was assumed to be one of the best choices to construct the graphene-based nanostructures with multi-catalyst nanoparticles well dispersed on graphene sheets, as it is hard to control the simultaneous homogenous growth of two or more components particles on graphene in one-step [37,43]. Herein, we develop a facile two-step strategy for green synthesis of RGO/Ag/CeO₂ nanocomposites, the schematic of which is illustrated in Fig. 1. Typically, GO/CeO₂ nanocomposites were first prepared via a self-assembly process, and then well-dispersed Ag nanoparticles with small size were in situ grown on RGO sheets. It is well known that GO sheets are highly negatively charged when dispersed in water, apparently as a result of ionization of the carboxyl and phenolic hydroxyl groups that exist on their surface. During the self-assembly process, AHA-stabilized CeO₂ nanoparticles were firstly prepared. The carboxylic acid of AHA would bond to the surface of CeO₂ nanoparticles and release a proton to form a carboxylate group. The proton would then protonate the amino group of AHA, generating a positively charged surface of the CeO₂ nanoparticles [4]. When AHA-stabilized CeO₂ nanoparticles and GO sheets with opposite charges were carefully introduced together, the mutual electrostatic interactions between these two components provide a strong driving force for the effective assembly of CeO₂ nanoparticles on GO sheets, forming well-combined nanocomposites. On the other hand, GO can serve as a mild reducing agent under alkaline conditions. The reducing ability of GO comes from the hydroxyl group attached to the hexagonal basal

plane, making it a phenolic entity [44]. It is known that phenolic protons are weakly acidic, and, under alkaline conditions, phenols undergo deprotonation to give phenolate anions. The active phenolate anions will transfer electrons to Ag⁺ forming metallic Ag through electrophilic aromatic substitution and are simultaneously transformed into semiquinone [45]. At the same time, GO can also convert into RGO under strong alkaline conditions [46]. Therefore, NaOH, the strong alkaline presented in our present system, plays a dual role: not only accelerating the reduction of Ag⁺ by GO to form Ag nanoparticles, but also inducing the reduction of GO into RGO. As a result, RGO/Ag/CeO₂ nanocomposites were formed finally.

3.2. Structural and morphological characterization

The typical XRD patterns and Raman spectra of the as-prepared graphite oxide, RGO, RGO/CeO₂ and RGO/Ag/CeO₂-3 nanocomposites are presented in Fig. 2. As shown in Fig. 2a, the original graphite oxide sample shows a strong diffraction peak centered at $2\theta = 10.3^\circ$, corresponding to the (001) reflection of graphite oxide [47]. In the XRD pattern of RGO nanosheets, the disappearance of the peak at $2\theta = 10.3^\circ$ confirms that the graphite oxide has been flaked to GO and then successfully reduced into RGO nanosheets. This XRD pattern is consistent with previous report for RGO sheets obtained from chemical reduction of GO by alkali [46]. For RGO/CeO₂ nanocomposites, the three characteristic peaks at 2θ values of 28.6° , 47.5° , 56.3° can be indexed to the (111), (220), (311) planes of cubic fluorite structured CeO₂ (JCPDS no. 34-0394). After decoration of RGO/CeO₂ with Ag nanoparticles, the XRD pattern additionally shows the (111), (200), (220) and (311) reflections of the face-centered cubic (fcc) phase Ag (JCPDS no.

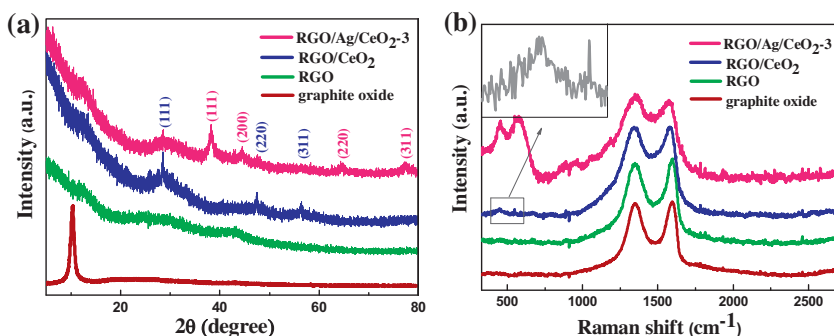


Fig. 2. (a) XRD patterns and (b) Raman spectra of graphite oxide, RGO, RGO/CeO₂ and RGO/Ag/CeO₂-3 nanocomposites. The inset in (b) is a local magnified view of Raman spectra of RGO/CeO₂.

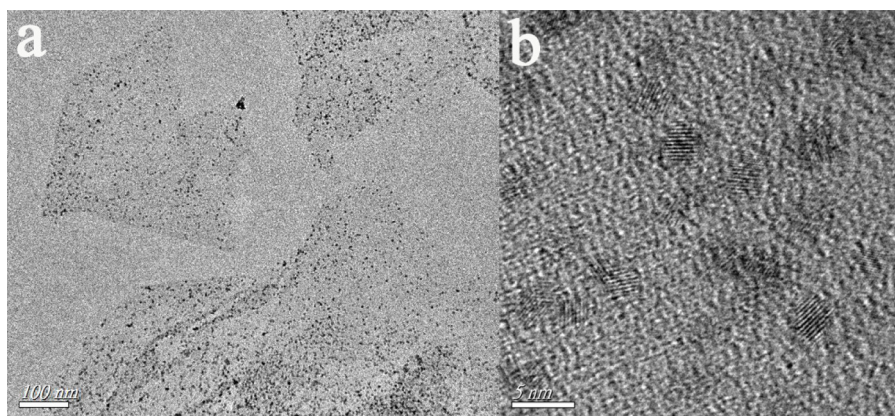


Fig. 3. TEM images of RGO/CeO₂ nanocomposites.

65–2871). This result indicates that metallic Ag nanoparticles have been successfully anchored to RGO/CeO₂ by reducing Ag⁺ ions in the presence of NaOH, forming RGO/Ag/CeO₂ nanocomposites.

Raman spectroscopy is a powerful and widely used tool to characterize the structural properties of graphene-based materials, such as disorder and defect structures. As shown in Fig. 2b, the Raman spectrum of graphite oxide displays two prominent peaks at 1347 and 1597 cm^{−1}, corresponding to the well-documented D and G bands, respectively. It is known that the D band is associated with structural defects and disorders that break the symmetry and selection rule, while the G band is usually assigned to the E_{2g} phonon of C sp² domains [48–51]. The intensity ratio of D–G band (I_D/I_G) is usually used as a measure of structural defects and disorder in graphitic structures [52–54]. Compared with graphite oxide (1.67), an increment in I_D/I_G was observed for bare RGO (1.92), indicating that more disordered carbon structure was produced after the exfoliation and reduction of graphite oxide. Besides the Raman peaks from the RGO, the peaks at 450 and 550 cm^{−1} in the RGO/CeO₂ nanocomposites can be assigned to the F_{2g} vibration mode of the anchored CeO₂ nanoparticles and the oxygen vacancies in the CeO₂ [55,56]. In addition, the I_D/I_G ratio for RGO/CeO₂ is further increased to 2.65, which suggests that an increase in the number of defects was brought by the introduction of CeO₂ nanoparticles on the RGO sheets [57]. This is possible because the attachment of CeO₂ nanoparticles on RGO stressed its surface and induced more defects [58]. After the loading of Ag nanoparticles, the intensity of Raman peaks of CeO₂ intensively increases as compared with that of RGO/CeO₂. This can be ascribed to the surface enhanced Raman scattering (SERS) from the intense local electromagnetic fields of Ag nanoparticles that accompanies plasmon resonance [59]. This fact further confirms that the effective combination of Ag nanoparticles and RGO/CeO₂ nanocomposites.

The detailed morphology, size and dispersivity of the particles on the surface of RGO were observed by TEM and high resolution TEM (HRTEM). Fig. 3 displays the representative (HR)TEM images of the RGO/CeO₂ nanocomposites, from which crumpled silk wave-like morphology that graphene intrinsically owns can be observed. Monodispersed CeO₂ nanoparticles are exclusively deposited on RGO sheets with highly uniform distribution, and the size of the CeO₂ nanoparticles is about 3 nm. The loaded amount of CeO₂ can be readily controlled by simply changing the dosages of the CeO₂ dispersion used during the self-assembly process [40]. It is clearly shown that CeO₂ nanoparticles are not dense enough to cover RGO sheets completely (Fig. 3a), and thus Ag nanoparticles can be deposited on the sites unoccupied by CeO₂. The TEM images of RGO/Ag/CeO₂-3 nanocomposites (Fig. 4a and b) show that the surface of RGO sheets was covered by a dense layer of Ag and CeO₂ nanoparticles, indicating that the method is efficient for producing

RGO/Ag/CeO₂ nanocomposites. The higher magnification TEM image shown in Fig. 4c clearly demonstrates the homogeneous distribution of Ag and CeO₂ particles on RGO. Additionally, acting as a “spacer”, the Ag and CeO₂ nanoparticles on the RGO can prevent the RGO sheets from aggregation and restacking. Highly dispersed metal nanoparticles on supports with large surface area have advantages in catalytic applications [60]. Although it is difficult to discern Ag and CeO₂ nanoparticles from each other due to their similar appearance in Fig. 4c, they can be distinguished based on the lattice spacing observed in the HRTEM image (Fig. 4d). The larger particles are Ag with particle size of about 10 nm, whereas the relatively small ones can be recognized as CeO₂ particles. The lattice spacings of 0.232 and 0.312 nm could be assigned to the (1 1 1) planes of Ag and (1 1 1) planes of CeO₂, respectively.

To identify the role of the CeO₂ in the synthesis of RGO/Ag nanocomposites, a control experiment was carried out under the same conditions without introducing CeO₂ dispersion into the reaction system, and the morphology of the product is shown in Fig. S1. It can be seen that Ag nanoparticles are also well deposited on the surface of RGO and some Ag nanoparticles tend to aggregate. The size of Ag nanoparticles is about 15 nm, which is larger than that in RGO/Ag/CeO₂-3 nanocomposites. This result indicates that the presence of CeO₂ has an influence on the size of Ag nanoparticles formed on RGO sheets. The reason for the smaller size of Ag nanoparticle in the RGO/Ag/CeO₂ nanocomposites can be proposed as follows: when the silver salts were introduced into the graphene oxide dispersion, Ag⁺ would attach to the surface of graphene oxide and serve as nucleation sites. After the introducing of NaOH, Ag⁺ ions were in situ reduced to form nuclei, while graphene oxide was reduced to RGO at the same time. It could be assumed that after positively charged CeO₂ nanoparticles were deposited on the surface of RGO, the electrostatic repulsion effect between CeO₂ and Ag⁺ favored the generation of much more nuclei and so the formation of smaller Ag nanoparticles. The size of Ag nanoparticles can be further decreased to about 8 nm when the feeding amount of CeO₂ dispersion was increased to 4 mL (RGO/Ag/CeO₂-4), as shown in Fig. S2.

In order to further clarify the surface characteristics of RGO/Ag/CeO₂ nanocomposites, the as-prepared samples were investigated using FT-IR spectroscopy and the results are shown in Fig. 5. The FT-IR spectrum of graphite oxide confirms the successful oxidation of graphite. In detail, the absorption bands at 3405 and 1403 cm^{−1} originate from stretching vibration and deformation vibration of O–H. The C=O stretching of COOH groups, stretching vibration peaks of C–OH and C–O are observed at 1727, 1224, and 1049 cm^{−1}, respectively. The peak at 1621 cm^{−1} is assigned to the vibrations of the adsorbed water molecules and also the contributions from the skeletal vibrations of unoxidized graphitic

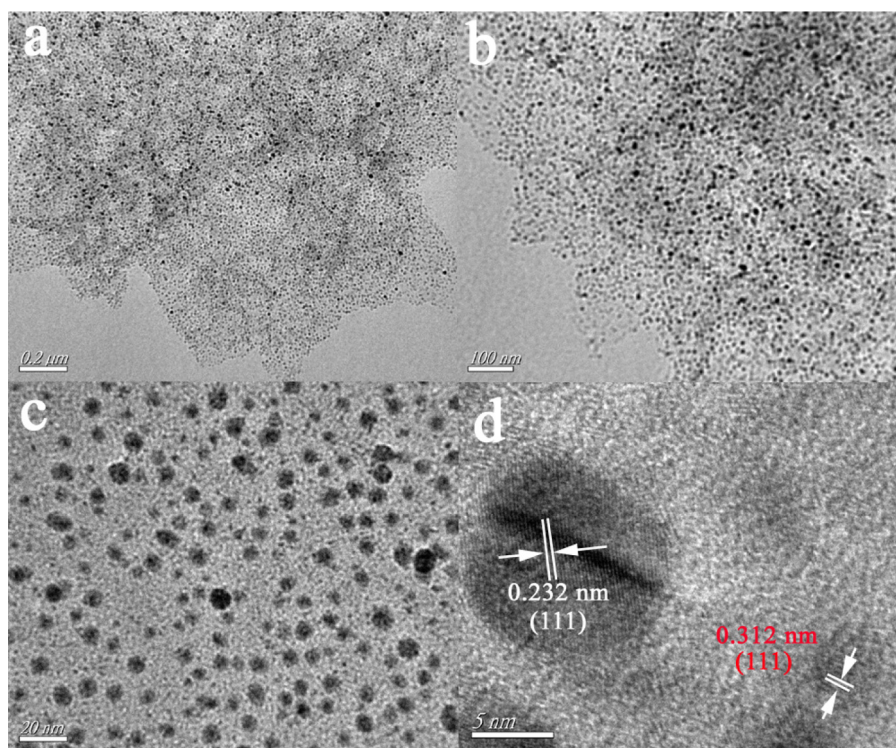


Fig. 4. (a–c) TEM and (d) HRTEM images of the RGO/Ag/CeO₂-3 nanocomposites.

domains [61]. In contrast, some of the peaks that related with the oxygen-containing functional groups decreased or even vanished in the FT-IR spectrum of bare RGO (Fig. 5c), revealing that the bulk of oxygen-containing functional groups were removed from GO after the reduction. The peak observed at about 1567 cm⁻¹ can be attributed to the skeletal vibration of the graphene sheets. Moreover, the peaks at 2920 and 2856 cm⁻¹ correspond to the asymmetric and symmetric C–H stretching vibrations of –CH₂– groups of PVP. Another peak at around 1655 cm⁻¹ ascribes to the C=O stretching of PVP amide unit. These results suggest that PVP molecules are adsorbed on the surface of RGO. Our previous work has demonstrated that PVP plays a significant role in improving the stability of GO/CeO₂ dispersions and in homogeneously loading CeO₂ nanoparticles onto RGO sheets [40]. To confirm the presence of AHA on the surface of RGO/Ag/CeO₂ nanocomposites, the FT-IR spectrum of the RGO/Ag/CeO₂ prepared in the absence of PVP is also

shown in Fig. 5d. The characteristic peaks of AHA can be observed, which suggests that there were chemical force interaction between AHA and the RGO/Ag/CeO₂ nanocomposites.

3.3. Catalytic properties toward *p*-nitrophenol

The reduction of aromatic nitro compounds to amines is a very important process in organic synthetic chemistry and in industrial preparation of many industrially important products. In this study, the catalytic properties of the RGO/Ag/CeO₂ nanocomposites were quantitatively evaluated with the reduction of *p*-nitrophenol into *p*-aminophenol by NaBH₄ as a model reaction, which was illustrated in Fig. 6a. This reaction has been demonstrated to be highly effective for the evaluation of catalytic activity of noble metals [4,62,63]. The original absorption peak of *p*-nitrophenol is at 317 nm and shifts to 400 nm immediately upon the addition of freshly prepared NaBH₄ solution, corresponding to a color change from light yellow to yellow-green due to the formation of *p*-nitrophenolate ions [64,65]. As the reduction reaction proceeds, the intensity of the absorption peak at 400 nm gradually decreases. Therefore, the reaction kinetics could be monitored easily from the time-dependent absorption spectra. Fig. 6b shows a typical UV–vis absorption change of the reaction system with RGO/Ag/CeO₂-3 ternary hybrid nanomaterials as the solid phase catalyst. It can be seen that the absorption at 400 nm associated with *p*-nitrophenol decreases with a concomitant appearance of a new peak at 300 nm, addressing the formation of *p*-aminophenol. When the reaction time up to 10 min, the peak due to the nitro compound was no longer observed, meaning that the catalytic reduction of *p*-nitrophenol had been completed. This could also be visually witnessed with the fading of the characteristic yellow color of the solution. However, although the reaction was a thermodynamically feasible process, it was kinetically restricted in the absence of a catalyst. Controlled experiments indicate that the reduction reaction did not occur in the absence of RGO/Ag/CeO₂-3 under the same other reaction conditions.

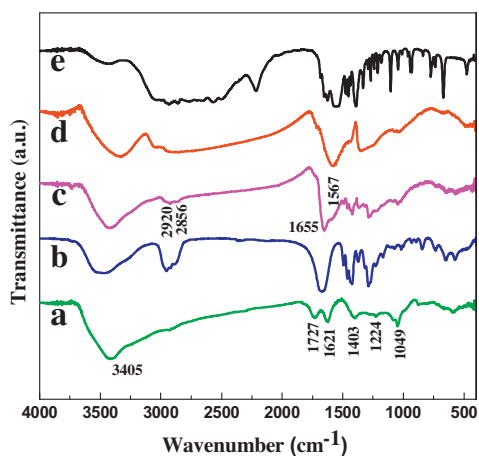


Fig. 5. FT-IR spectra of (a) graphite oxide, (b) PVP, (c) bare RGO, (d) RGO/Ag/CeO₂ nanocomposites prepared in the absence of PVP, and (e) AHA.

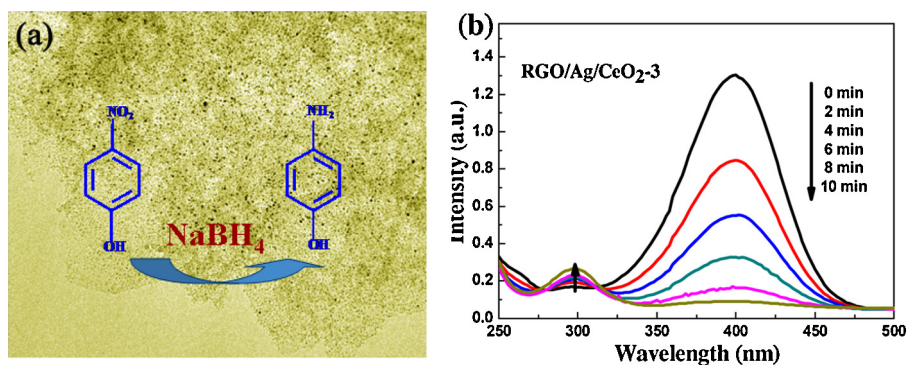


Fig. 6. (a) Illustration and (b) successive UV-vis spectra for the reduction of *p*-nitrophenol by NaBH_4 with RGO/Ag/CeO₂-3 nanocomposite as a catalyst.

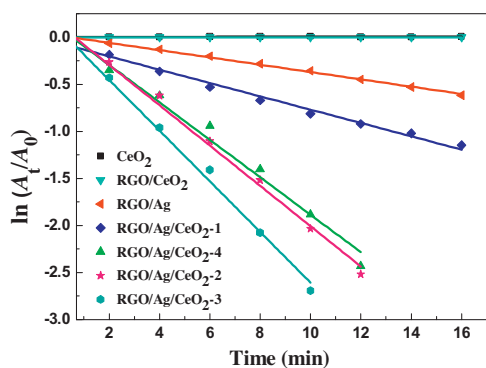


Fig. 7. Pseudo first order plots of $\ln(A_t/A_0)$ versus reaction time for the reduction of *p*-nitrophenol catalyzed over different catalysts.

The UV-vis spectra also exhibit an isosbestic point between two absorption bands (Fig. 6b and Fig. S3), indicating that only two principal species, *p*-nitrophenol and *p*-aminophenol, influence the reaction kinetics [66,67]. Therefore, pseudo first order kinetics could be applied for the evaluation of rate constants when excess NaBH_4 was used [66]. The ratio of C_t and C_0 , where C_t and C_0 are *p*-nitrophenol concentrations at time t and 0, respectively, was measured from the relative intensity of the respective absorbances, A_t/A_0 . The relations of $\ln(A_t/A_0)$ (at peak of 400 nm) versus t under different catalysts are shown in Fig. S4 and Fig. 7. It is clear that $\ln(A_t/A_0)$ shows a good linear correlation ($R^2 > 0.98$) with the reaction time for all catalysts, indicating that the reactions follow first-order kinetics. The rate constants for different catalysts were estimated from diffusion-coupled first order reaction kinetics using the slopes of the straight lines and the corresponding results are listed in Table 1. It was found that the increase of the Ag content within a certain range is helpful to enhance the catalytic efficiency. It is mainly because the more Ag nanoparticles are deposited, the more reaction sites are provided in the composite materials, which lead to a higher reaction rate [10]. As evidenced

by TEM images in Fig. S5, Ag nanoparticles with bigger size were formed when the loaded amount of Ag is too high. As a result, the RGO/Ag nanocomposites with high Ag content show decreased catalytic activities. Since RGO/Ag nanocomposites prepared with 20 mg of AgNO_3 exhibit the highest catalytic activity, we discuss herein the data related to the RGO/Ag/CeO₂ catalysts prepared with 20 mg of AgNO_3 . The rate constants show that the catalytic activities of RGO/Ag/CeO₂ and RGO/Ag nanocomposites increase in the following order: RGO/Ag < RGO/Ag/CeO₂-1 < RGO/Ag/CeO₂-4 < RGO/Ag/CeO₂-2 < RGO/Ag/CeO₂-3. It is worthwhile noting that the catalytic activity of RGO/Ag nanocomposites can be remarkably improved by combining with CeO₂ nanoparticles. In addition, since RGO and free CeO₂ both do not show obvious catalytic activity (Fig. 7 and Fig. S4), it is deduced that the catalytic activity of RGO/Ag/CeO₂ nanocomposites originates from Ag, while RGO and CeO₂ serve as synergists. It seems that the size of Ag nanoparticles has an important effect on the catalytic activity. Previous study has demonstrated that a decrease of the metal particle size leads to an increase in the fraction of low coordination metal sites such as vertices and edges, which can facilitate the reduction of *p*-nitrophenol [67]. Thus the catalysts of RGO/Ag/CeO₂ with smaller Ag particles have higher catalytic activities than RGO/Ag nanocomposites. However, if the content of CeO₂ is too high in the nanocomposites, a decrease of the activities occurs, as evidenced by RGO/Ag/CeO₂-3 and RGO/Ag/CeO₂-4. We consider that the decreased catalytic performance of RGO/Ag/CeO₂-4 nanocomposites is attributable to the following factor: RGO sheets have high adsorption ability toward *p*-nitrophenol via π - π stacking interactions. This provides a high concentration of *p*-nitrophenol near to the Ag nanoparticles on RGO, leading to efficient contact between them [68]. In the nanocomposites, Ag and CeO₂ nanoparticles are tightly attached to the surfaces of the RGO sheets (Fig. S2). With further increase of CeO₂ content, the RGO sheets might be completely covered by excessive nanoparticles which would hinder the adsorption of RGO toward *p*-nitrophenol, and thus decrease the catalytic activity. This result reveals that a suitable loading amount of CeO₂ is crucial for optimizing the catalytic activity of RGO/Ag/CeO₂ nanocomposites.

As is known, catalysts based on noble metal nanoparticles often suffer from poisoning by the reaction product during the catalytic process [6,69]. Thus, the improvement of the catalytic stability is the top priorities for practical applications. In order to test the catalytic stability of RGO/Ag/CeO₂-3 nanocomposites, the catalyst was recycled up to five times and the rate constants for the successive five cycles is shown in Fig. 8a. It can be seen that the catalytic efficiency only displays a slight decrease after five cycles, indicating the excellent stability of the composite catalyst against poisoning by the product of the reaction. In contrast, the RGO/Ag catalyst dramatically lost its catalytic activity over the course of each round of reaction. These experimental results exhibit that the loading of CeO₂ nanoparticles effectively improves the stability of

Table 1

The experimental details, rate constants for the reduction reaction of *p*-nitrophenol and the correlation coefficient for $\ln(A_t/A_0)$ - t plots under different catalysts.

Samples	AgNO_3 (mg)	CeO ₂ (mL)	Ag content (wt%)	K (min ⁻¹)	R^2
RGO/Ag-1	10	0	11.0	0.0217	0.9986
RGO/Ag	20	0	20.3	0.0388	0.9965
RGO/Ag-2	30	0	25.7	0.0288	0.9997
RGO/Ag/CeO ₂ -1	20	1	18.9	0.0708	0.9876
RGO/Ag/CeO ₂ -2	20	2	16.7	0.214	0.9901
RGO/Ag/CeO ₂ -3	20	3	14.6	0.269	0.9924
RGO/Ag/CeO ₂ -4	20	4	13.6	0.199	0.9812

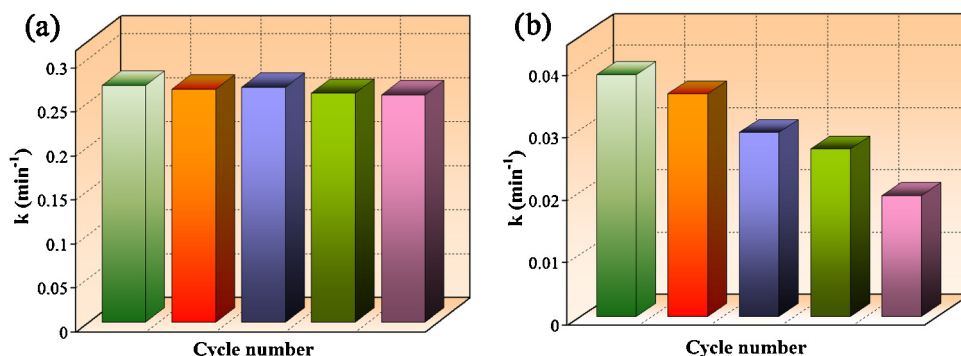


Fig. 8. The catalytic performance within five cycles for (a) RGO/Ag/CeO₂-3 and (b) RGO/Ag catalysts.

the RGO/Ag catalysts. The superior stability of our RGO/Ag/CeO₂-3 nanocomposites can be assumed to involve a similar mechanism to that reported by Xia et al. [4]. The residual AHA on the surface of the RGO/Ag/CeO₂-3 nanocomposites, as evidenced by the FT-IR spectrum, enables them to avoid the strong adsorption toward *p*-aminophenol product, and thus the nanocomposites exhibit a good catalytic stability [4]. Some other factors might also play an important role in their catalytic stability, such as surface passivation by other chemical species in the catalytic reaction and synergistic effect between CeO₂ and Ag [23]. In addition, due to the smaller size, the nanoparticle catalysts are generally hard to be recycled. Our RGO/Ag/CeO₂ nanocomposite catalysts overcome this problem because they could be easily separated and recollected via centrifugation due to the presence of the RGO.

4. Conclusions

In summary, RGO/Ag/CeO₂ ternary nanocomposites have been successfully prepared through an environmentally friendly two-step strategy, and their microstructure and catalytic properties toward the reduction of *p*-nitrophenol by NaBH₄ are investigated. It is shown that CeO₂ and Ag nanoparticles are uniformly deposited on the surface of RGO sheets, and the presence of CeO₂ can decrease the size of the Ag nanoparticles formed on RGO. The catalytic experimental results indicate that the incorporation CeO₂ with RGO/Ag nanocomposites can significantly enhance the catalytic activity and stability of the composite catalysts. Moreover, a suitable loading amount of Ag and CeO₂ on RGO is found to be crucial for optimizing the catalytic activity of the nanocomposites. It is expected that the synthesis of RGO/Ag/CeO₂ ternary hybrid materials will pave a way to design other graphene-based multi-component composites for various applications.

Acknowledgements

The authors are grateful for financial support from the National Natural Science Foundation of China (Nos. 51272094, 51072071 and 51102117) and Doctoral Innovation Program Foundation of Jiangsu Province (CXLX12.0633).

Appendix A. Supplementary data

Supplementary data associated with this article can be found, in the online version, at <http://dx.doi.org/10.1016/j.apcatb.2013.07.052>.

References

- [1] M.S. Yavuz, Y.Y. Cheng, J.Y. Chen, C.M. Cobley, Q. Zhang, M. Rycenga, J.W. Xie, C. Kim, K.H. Song, A.G. Schwartz, L.H.V. Wang, Y.N. Xia, *Nat. Mater.* 8 (2009) 935–939.
- [2] B. Lim, M.J. Jiang, P.H.C. Camargo, E.C. Cho, J. Tao, X.M. Lu, Y.M. Zhu, Y.N. Xia, *Science* 324 (2009) 1302–1305.
- [3] A. Halder, S. Patra, B. Viswanath, N. Munichandraiah, N. Ravishankar, *Nanoscale* 3 (2011) 725–730.
- [4] T.Y. Yu, J. Zeng, B. Lim, Y.N. Xia, *Adv. Mater.* 22 (2010) 5188–5192.
- [5] S.J. Guo, S.J. Dong, E.K. Wang, *Adv. Mater.* 22 (2010) 1269–1272.
- [6] F.H. Lin, R.A. Doong, *J. Phys. Chem. C* 115 (2011) 6591–6598.
- [7] J.F. Shen, M. Shi, B. Yan, H.W. Ma, N. Li, M.X. Ye, *J. Mater. Chem.* 21 (2011) 7795–7801.
- [8] R. Prucek, J. Tucek, M. Kilianova, A. Panacek, L. Kvitek, J. Filip, M. Kolar, K. Tomankova, R. Zboril, *Biomaterials* 32 (2011) 4704–4713.
- [9] X.Q. Fu, F.L. Bei, X. Wang, S. O'Brien, J.R. Lombardi, *Nanoscale* 2 (2010) 1461–1466.
- [10] J.C. Qu, C.L. Ren, Y.L. Dong, Y.P. Chang, M. Zhou, X.G. Chen, *Chem. Eng. J.* 211/212 (2012) 412–420.
- [11] Y.G. Sun, Y.N. Xia, *Science* 298 (2002) 2176–2179.
- [12] P. Zhang, C.L. Shao, Z.Y. Zhang, M.Y. Zhang, J.B. Mu, Z.C. Guo, Y.C. Liu, *Nanoscale* 3 (2011) 3357–3363.
- [13] X.Y. Li, X. Wang, S.Y. Song, D.P. Liu, H.J. Zhang, *Chem. Eur. J.* 18 (2012) 7601–7607.
- [14] I. Lee, F. Delbecq, R. Morales, M.A. Albiter, F. Zaera, *Nat. Mater.* 8 (2009) 132–138.
- [15] A. Murugadoss, A. Chattopadhyay, *Nanotechnology* 19 (2008) 015603.
- [16] Z.P. Qu, W.X. Huang, M.J. Cheng, X.H. Bao, *J. Phys. Chem. B* 109 (2005) 15842–15848.
- [17] Y. Guo, M. Sakurai, H. Kameyama, *Appl. Catal. B* 79 (2008) 382–393.
- [18] M. Choi, Z.J. Wu, E. Iglesia, *J. Am. Chem. Soc.* 132 (2010) 9129–9137.
- [19] K. Shimizu, H. Kawachi, S. Komai, K. Yoshida, Y. Sasaki, A. Satsuma, *Catal. Today* 175 (2011) 93–99.
- [20] H. Sakai, T. Kanda, H. Shibata, T. Ohkubo, M. Abe, *J. Am. Chem. Soc.* 128 (2006) 4944–4945.
- [21] L.M. Chen, D. Ma, X.H. Bao, *J. Phys. Chem. C* 111 (2007) 2229–2234.
- [22] N. Tanaka, H. Nishikiori, S. Kubota, M. Endo, T. Fujii, *Carbon* 47 (2009) 2752–2754.
- [23] C.Z. Zhu, P. Wang, L. Wang, L. Han, S.J. Dong, *Nanoscale* 3 (2011) 4376–4382.
- [24] S.J. Guo, S.J. Dong, *Chem. Soc. Rev.* 40 (2011) 2644–2672.
- [25] P. Avouris, Z.H. Chen, V. Perebeinos, *Nat. Nanotechnol.* 2 (2007) 605–615.
- [26] J.H. Chen, C. Jiang, S. Xiao, M. Ishigami, M.S. Fuhrer, *Nat. Nanotechnol.* 3 (2008) 206–209.
- [27] A. Peigney, C. Laurent, E. Flahaut, R.R. Bacsa, A. Rousset, *Carbon* 39 (2001) 507–514.
- [28] A.K. Geim, K.S. Novoselov, *Nat. Mater.* 6 (2007) 183–191.
- [29] A.K. Geim, *Science* 324 (2009) 1530–1534.
- [30] J.G. Hou, C. Yang, Z. Wang, S.Q. Jiao, H.M. Zhu, *Appl. Catal. B* 129 (2013) 333–341.
- [31] E. Antolini, *Appl. Catal. B* 123 (2012) 52–68.
- [32] Y.M. Zhang, X. Yuan, Y. Chen, J. Mater. Chem. 22 (2012) 7245–7251.
- [33] T.S. Wu, S. Liu, Y.L. Luo, W.B. Lu, L. Wang, X.P. Sun, *Nanoscale* 3 (2011) 2142–2144.
- [34] X.Y. Qin, Y.L. Luo, W.B. Lu, G.H. Chang, A.M. Asiri, A.O. Al-Youbi, X.P. Sun, *Electrochim. Acta* 79 (2012) 46–51.
- [35] J.Q. Tian, S. Liu, Y.W. Zhang, H.Y. Li, L. Wang, Y.L. Luo, A.M. Asiri, A.O. Al-Youbi, X.P. Sun, *Inorg. Chem.* 51 (2012) 4742–4746.
- [36] H. Zhao, H.G. Fu, T.S. Zhao, L. Wang, T.X. Tan, *J. Colloid Interface Sci.* 375 (2012) 30–34.
- [37] D.H. Yoo, T.V. Cuong, V.H. Luan, N.T. Khoa, E.J. Kim, S.H. Hur, S.H. Hahn, *J. Phys. Chem. C* 116 (2012) 7180–7184.
- [38] S. Ghasemi, S.R. Setayesh, A. Habibi-Yangjeh, M.R. Hormozi-Nezhad, M.R. Gholami, *J. Hazard. Mater.* 199 (2012) 170–178.
- [39] J.G. Hou, C. Yang, Z. Wang, S.Q. Jiao, H.M. Zhu, *Appl. Catal. B* 129 (2013) 333–341.
- [40] Z.Y. Ji, X.P. Shen, M.Z. Li, H. Zhou, G.X. Zhu, K.M. Chen, *Nanotechnology* 24 (2013) 115603.
- [41] W.S. Hummers, R.E. Offeman, *J. Am. Chem. Soc.* 80 (1958) 1339.
- [42] Z.Y. Ji, X.P. Shen, G.X. Zhu, H. Zhou, A.H. Yuan, *J. Mater. Chem.* 22 (2012) 3471–3477.
- [43] P. Wang, L. Han, C.Z. Zhu, Y.M. Zhai, S.J. Dong, *Nano Res.* 4 (2011) 1153–1162.

- [44] P.R. Selvakannan, A. Swami, D. Srisathiyarayanan, P.S. Shirude, R. Pasricha, A.B. Mandale, M. Sastry, *Langmuir* 20 (2004) 7825–7836.
- [45] R. Pasricha, S. Gupta, A.K. Srivastava, *Small* 5 (2009) 2253–2259.
- [46] X.B. Fan, W.C. Peng, Y. Li, X.Y. Li, S.L. Wang, G.L. Zhang, F.B. Zhang, *Adv. Mater.* 20 (2008) 4490–4493.
- [47] T. Nakajima, A. Mabuchi, R. Hagiwara, *Carbon* 26 (1988) 357–361.
- [48] F. Tuinstra, J.L. Koenig, *J. Chem. Phys.* 53 (1970) 1126–1130.
- [49] D. Graf, F. Molitor, K. Ensslin, C. Stampfer, A. Jungen, C. Hierold, L. Wirtz, *Nano Lett.* 7 (2007) 238–242.
- [50] A.C. Ferrari, J.C. Meyer, V. Scardaci, C. Casiraghi, M. Lazzeri, F. Mauri, S. Piscanec, D. Jiang, K.S. Novoselov, S. Roth, A.K. Geim, *Phys. Rev. Lett.* 97 (2006) 187401.
- [51] A. Barras, M.R. Das, R.R. Devarapalli, M.V. Shelke, S. Cordier, S. Szunerits, R. Boukherroub, *Appl. Catal. B* 130 (2013) 270–276.
- [52] M.S. Dresselhaus, A. Jorio, M. Hofmann, G. Dresselhaus, R. Saito, *Nano Lett.* 10 (2010) 751–758.
- [53] M.M. Lucchese, F. Satavle, E.H. Martins Ferreira, C. Vilani, M.V.O. Moutinho, R.B. Capaz, C.A. Achete, A. Jorio, *Carbon* 48 (2010) 1592–1597.
- [54] C.N.R. Rao, A.K. Sood, K.S. Subrahmanyam, A. Govindaraj, *Angew. Chem. Int. Ed.* 48 (2009) 7752–7777.
- [55] D. Joung, V. Singh, S. Park, A. Schulte, S. Seal, S.I. Khondaker, *J. Phys. Chem. C* 115 (2011) 24494–24500.
- [56] B.M. Reddy, G. Thrimurthulu, L. Katta, Y. Yamada, S.E. Park, *J. Phys. Chem. C* 113 (2009) 15882–15890.
- [57] B. Krauss, T. Lohmann, D.H. Chae, M. Haluska, K. von Klitzing, J.H. Smet, *Phys. Rev. B: Condens. Matter Mater. Phys.* 79 (2009) 165428.
- [58] Y.Y. Wen, H.M. Ding, Y.K. Shan, *Nanoscale* 3 (2011) 4411–4417.
- [59] J. Li, C.Y. Liu, *Eur. J. Inorg. Chem.* (2010) 1244–1248.
- [60] Z.Y. Ji, X.P. Shen, G.X. Zhu, K.M. Chen, G.H. Fu, L. Tong, *J. Electroanal. Chem.* 682 (2012) 95–100.
- [61] Y.X. Xu, H. Bai, G.W. Lu, C. Li, G.Q. Shi, *J. Am. Chem. Soc.* 130 (2008) 5856–5857.
- [62] M. Schrinner, M. Ballauff, Y. Talmon, Y. Kauffmann, J. Thun, M. Moller, J. Breu, *Science* 323 (2009) 617–620.
- [63] Y. Mei, Y. Lu, F. Polzer, M. Ballauff, M. Drechsler, *Chem. Mater.* 19 (2007) 1062–1069.
- [64] S. Praharaj, S. Nath, S.K. Ghosh, S. Kundu, T. Pal, *Langmuir* 20 (2004) 9889–9892.
- [65] J. Zeng, Q. Zhang, J.Y. Chen, Y.N. Xia, *Nano Lett.* 10 (2010) 30–35.
- [66] K.L. Wu, X.W. Wei, X.M. Zhou, D.H. Wu, X.W. Liu, Y. Ye, Q. Wang, *J. Phys. Chem. C* 115 (2011) 16268–16274.
- [67] J. Lee, J.C. Park, H. Song, *Adv. Mater.* 20 (2008) 1523–1528.
- [68] J. Li, C.Y. Liu, Y. Liu, *J. Mater. Chem.* 22 (2012) 8426–8430.
- [69] R. Narayanan, M.A. El-Sayed, *J. Am. Chem. Soc.* 125 (2003) 8340–8347.